

Correspondence of defect energy levels in hybrid density functional theory and many-body perturbation theory

Wei Chen and Alfredo Pasquarello

Chaire de Simulation à l'Echelle Atomique (CSEA), Ecole Polytechnique Fédérale de Lausanne (EPFL), CH-1015 Lausanne, Switzerland

(Received 23 May 2013; revised manuscript received 16 August 2013; published 3 September 2013)

We demonstrate the correspondence between charge transition levels of localized point defects in hybrid density functional theory and in G_0W_0 many-body perturbation theory. To achieve this correspondence, it is necessary to properly combine the treatments of the finite-size effect, the delocalization error, and the path dependency in the G_0W_0 scheme. In particular, we introduce a beyond-monopole finite-size electrostatic correction for the eigenvalue which is fully consistent with the analogous correction for the total energy. We illustrate how the comparison with experiment is affected by the calculated band-edge positions, which unlike the defect levels are sensitive to the adopted electronic-structure method.

DOI: [10.1103/PhysRevB.88.115104](https://doi.org/10.1103/PhysRevB.88.115104)

PACS number(s): 71.15.Mb, 31.15.E-, 71.55.-i

I. INTRODUCTION

Theoretical predictions of defect energy levels play an integral part in the understanding of point defects in semiconductors and insulators. One is often interested in the thermodynamic transition level $\mu(q/q')$, the Fermi level at which two charge states q and q' have the same total energy. Experimentally, such levels are referenced with respect to the band edges. Despite its huge dominance in atomic-scale simulations, Kohn-Sham (KS) density functional theory (DFT) within the semilocal approximation struggles to give convincing defect levels, as the predicted band gaps are subject to severe underestimations. Various techniques have been proposed to circumvent the “band-gap problem,” among which hybrid density functionals within the generalized KS scheme have now become the method of choice in the study of defect properties.¹ For deep defect centers, it has been found that semilocal functionals yield charge transition levels in accord with hybrid-functional calculations, provided the energy levels are referred to the local electrostatic potential rather than to the band edges.² This is now well understood as the total energy of finite systems is reasonably accurate with approximate density functionals when evaluated at integer number of electrons.³ The error in $\mu(q/q')$ obtained from semilocal functionals thereby mostly lies in the problematic band-edge positions.⁴

As a more rigorous approach, many-body perturbation theory has been recently introduced to defect calculations via a reformulation of $\mu(q/q')$ in terms of electronic and geometrical contributions.⁵ In practice, the vertical (optical) transition level $\mu^{\text{opt}}(q/q')$ is directly tackled by the perturbative G_0W_0 approximation in terms of quasiparticle (QP) removal or addition energies,^{6,7} whereas the structural relaxation is described within DFT. This combined scheme has been applied to various defects in an effort to achieve a more accurate description of their energy levels.^{8–12} However, in specific cases, significant discrepancies have been found with respect to previous results obtained with hybrid functionals. For instance, it has been demonstrated that the GW defect levels of the O interstitial in amorphous SiO_2 differ from their corresponding hybrid-functional levels by more than 3 eV.⁹ Similarly, differences exceeding 1 eV have been found for the charge transition levels of the O vacancy in HfO_2 .^{8,13} This situation severely questions the validity of hybrid functionals

for predicting defect levels in the band gap, at a time in which the use of such methods is strongly growing.^{1,14}

In this work, we demonstrate that G_0W_0 quasiparticle energy levels of localized defects closely correspond to charge transition levels obtained through total-energy differences within hybrid DFT. To reach this conclusion, it is necessary to properly address several aspects peculiar to the G_0W_0 scheme, including finite-size effects, the delocalization error affecting vertical transitions, and the path dependency resulting from the combination with DFT structural relaxations. Furthermore, we highlight that the comparison of charge transition levels with experiment is mediated by the band-edge positions which unlike the defect levels are sensitive to the adopted electronic-structure scheme.

This paper is organized as follows. The calculation details are presented in Sec. II. In Sec. III, we address important issues underlying the G_0W_0 scheme. The correspondence of defect energy levels is presented in Sec. IV. We also illustrate the role of the band-edge positions through a comparison with experiment. Finally, the conclusions are drawn in Sec. V.

II. COMPUTATIONAL METHODS

Three point defects are studied in this work: the fluorine vacancy V_F (color center) in LiF ($q = 0, 1$), the oxygen interstitial O_{int} in α -quartz SiO_2 ($q = 0, -1, -2$), and the carbon split interstitial with $\langle 100 \rangle$ orientation $C_{\text{sp}(100)}$ in cubic 3C-SiC ($q = 0, 1, 2$). This choice of defects spans atomically localized defects in ionic insulators and covalent semiconductors. In particular, the oxygen interstitial defect in SiO_2 allows us to inspect the detailed origin of the large discrepancy found in Ref. 9. The charge transition levels are calculated within the supercell approach, with a 64-atom LiF, a 72-atom α -quartz, and a 64-atom 3C-SiC supercell. We use DFT calculations based on the semilocal Perdew-Burke-Ernzerhof (PBE) exchange-correlation functional¹⁵ to obtain the relaxed defect structures used throughout this work. All the DFT calculations involve plane-wave basis sets and norm-conserving pseudopotentials (NCPPs), as provided in the QUANTUM-ESPRESSO suite.¹⁶

The hybrid-functional calculations are performed with the PBE0 (Ref. 17) and the range-separated Heyd-Scuseria-

TABLE I. Band gaps (E_g) of LiF, α -quartz SiO₂, and 3C-SiC calculated in PBE, PBE0, HSE, and G_0W_0 . The fractions of Fock exchange α reproducing the G_0W_0 band gap in the hybrid-functional calculations are given.

	E_g (eV)				α	
	PBE	PBE0	HSE	G_0W_0	PBE0	HSE
LiF	8.85	11.85	11.11	13.25	0.35	0.47
SiO ₂	5.66	8.21	7.48	8.77	0.31	0.43
SiC	1.40	3.01	2.27	2.25	0.13	0.25

Ernzerhof¹⁸ (HSE) functionals. We use the HSE implementation and treat the exchange potential as described in Refs. 19 and 20, respectively. To ease the comparison, the fraction of Fock exchange α is adapted to reproduce the G_0W_0 quasiparticle gaps (LiF: 13.2 eV, α -quartz: 8.9 eV, 3C-SiC: 2.3 eV). The adopted values are given in Table I. The charge transition levels are obtained through total-energy differences.²¹ The valence-band maximum (VBM) of the pristine bulk is positioned with respect to the defect system through an electrostatic-potential alignment.²² We correct the total energy using the finite-size electrostatic correction proposed by Freysoldt, Neugebauer, and Van de Walle:^{23,24}

$$E_{\text{corr}} = E_{\text{Mad}}^{\text{pc}} - q \Delta V_{q/0}^{\text{DFT/pc}}, \quad (1)$$

where $E_{\text{Mad}}^{\text{pc}}$ is the Madelung energy of a point charge embedded in a dielectric,²⁵ and $\Delta V_{q/0}^{\text{DFT/pc}}$ is the alignment between the DFT potential (charged versus neutral) and the point-charge potential evaluated far away from the defect. A detailed discussion of Eq. (1) is given in Appendix A. Such finite-size corrections are systematically included in all the total-energy differences obtained within the semilocal and hybrid density functional schemes. For Li, we include the 1s electrons among the valence states. A $2 \times 2 \times 2$ \mathbf{k} -point sampling is used throughout this work, whereas for SiO₂ and SiC the \mathbf{k} points are shifted off the Γ point (cf. Table II).

The G_0W_0 calculations are achieved with the projector-augmented wave (PAW) method²⁶ as found in the ABINIT implementation,²⁷ using PBE orbitals and eigenvalues as a starting point. We set stringent conditions on computational parameters such as the energy cutoff and the number of unoccupied states, aiming at energy levels converged within 0.1 eV. In the G_0W_0 calculations of vertical transitions, the Godby-Needs plasmon-pole model is used for the dielectric

TABLE II. Adopted parameters in PBE, PBE0, HSE, and PBE + G_0W_0 : ground-state cutoff energy E_{cut} (in Ry), \mathbf{k} -point mesh, \mathbf{q} -point samplings in the Fock exchange evaluation and the G_0W_0 self-energy calculation, number of (occupied and unoccupied) bands N_b , and the cutoff energy $E_{\text{cut}}^{\text{eps}}$ (in Ry) used in the dielectric matrix.

	(Hybrid) DFT			G_0W_0			
	E_{cut}	\mathbf{k} points	\mathbf{q} points	E_{cut}	\mathbf{q} points	$E_{\text{cut}}^{\text{eps}}$	N_b
LiF: V_F	150	$2 \times 2 \times 2$	$1 \times 1 \times 1$	70	$2 \times 2 \times 2$	20	1800
SiO ₂ : O_{int}	80	$2 \times 2 \times 2^a$	$1 \times 1 \times 1$	66	$2 \times 2 \times 2$	15	3000
SiC: C_{sp}	54	$2 \times 2 \times 2^a$	$2 \times 2 \times 2$	56	$2 \times 2 \times 2$	20	2000

^aShifted off the Γ point.

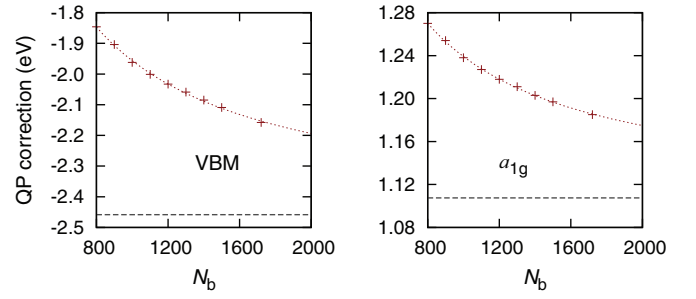


FIG. 1. (Color online) The convergence of the quasiparticle (QP) correction with respect to the number of bands N_b used in the self-energy for an F^+ center in LiF. QP corrections are given for the VBM and the a_{1g} defect level. The extrapolation limits are shown as horizontal dashed lines. A 63-atom supercell is used and the neutral defect geometry is assumed.

screening in which the high-lying unoccupied states (up to 100 eV above the VBM) are included.²⁸ The detailed parameters are given in Table II. The self-energy is extrapolated to infinite unoccupied states using a hyperbolic function to overcome the slow convergence,²⁹

$$\varepsilon^{\text{QP}}(N_b) = \varepsilon_0 + \frac{a}{N_b - N_0}, \quad (2)$$

where a and N_0 are fitting parameters, and ε_0 is the extrapolation limit. The extrapolation scheme is presented in Fig. 1 for the F^+ center in LiF.

We also checked that the G_0W_0 results do not depend on whether an NCPP or a PAW scheme is adopted as long as the semicore states are properly accounted for. We present in Fig. 2 G_0W_0 defect energy levels of the F center in LiF as obtained within the NCPP and PAW methods. Compared to the PAW results, the NCPP shifts both the VBM and the defect levels by ~ -0.1 eV. Consequently, this gives rise to a difference of 0.12 eV between the two charge transition levels when the average electrostatic potential is taken as reference. We assign this difference to residual numerical inaccuracies of the two schemes.

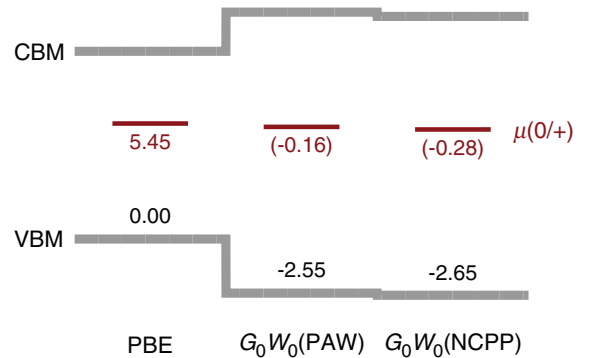


FIG. 2. (Color online) G_0W_0 defect energy levels $\mu(0/+)$ of the F center in LiF as calculated within PAW and NCPP schemes, in comparison to PBE results. The calculations are aligned with respect to the electrostatic potential of the pristine bulk. Values in parentheses show the shifts with respect to the PBE defect levels. Energies are in eV.

III. ISSUES UNDERLYING THE G_0W_0 SCHEME

A. Finite-size correction

Apart from the computational parameters, the G_0W_0 calculations include several other issues which need to be addressed. One important issue is the treatment of finite-size effects. In the G_0W_0 calculations, one identifies two contributions: one resulting from the scaling of the Kohn-Sham *eigenvalue* in the PBE calculation,^{8,10,22} and one associated with the GW quasiparticle correction.

We first address the finite-size effect on the PBE eigenvalue. For the purpose of comparison, it is important to correct the eigenvalue in a consistent way with respect to the correction of the total energy in the hybrid-functional calculations. We thus express the eigenvalue correction for a defect level ψ_d as $\langle \psi_d | v_{\text{corr}}^{\text{KS}}(\mathbf{r}) | \psi_d \rangle$, where the Kohn-Sham potential correction $v_{\text{corr}}^{\text{KS}}(\mathbf{r})$ is the functional derivative of the total-energy correction E_{corr} with respect to the charge density n_e (Refs. 22 and 30):

$$v_{\text{corr}}^{\text{KS}}(\mathbf{r}) = \frac{\delta E_{\text{corr}}}{\delta n_e(\mathbf{r})}. \quad (3)$$

Without loss of generality, we consider the correction for cubic supercells. Using the total-energy correction of Eq. (1), we have

$$v_{\text{corr}}^{\text{KS}}(\mathbf{r}) = -\frac{\alpha q}{\varepsilon L} - \frac{\delta(q \Delta V_{q/0}^{\text{DFT/pc}})}{\delta n_e(\mathbf{r})}, \quad (4)$$

where $L = \Omega^{-1/3}$ is the size of the supercell, and ε the dielectric constant. Neglecting local effects in the DFT potential, we write $\Delta V_{q/0}^{\text{DFT/pc}}$ as²²

$$\Delta V^{\text{DFT/pc}} \approx \frac{2\pi}{3\varepsilon\Omega} \int r^2 \rho_d(\mathbf{r}) d\mathbf{r}, \quad (5)$$

where ρ_d corresponds to a model charge distribution fitted to the defect charge density. The origin is chosen so that the contribution of the dipole vanishes. This leads to the following correction to the KS potential^{22,31}

$$v_{\text{corr}}^{\text{KS}}(\mathbf{r}) = -\frac{\alpha q}{\varepsilon L} + \frac{2\pi}{3\varepsilon\Omega} \int r^2 \rho_d(\mathbf{r}) d\mathbf{r} + \frac{2\pi}{3\varepsilon\Omega} q r^2. \quad (6)$$

Assuming that only one KS defect level is involved in the charging process, we express the defect charge density $\rho_d(\mathbf{r})$ in terms of the defect wave function ψ_d via $\rho_d(\mathbf{r}) = q |\psi_d(\mathbf{r})|^2$. The correction to the specific KS defect level is then given by

$$\begin{aligned} \varepsilon_{d,\text{corr}}^{\text{KS}} &= \langle \psi_d(\mathbf{r}) | v_{\text{corr}}^{\text{KS}}(\mathbf{r}) | \psi_d(\mathbf{r}) \rangle \\ &= -\frac{\alpha q}{\varepsilon L} + \frac{2\pi}{3\varepsilon\Omega} \left[\int r^2 \rho_d(\mathbf{r}) d\mathbf{r} + q \langle \psi_d(\mathbf{r}) | r^2 | \psi_d(\mathbf{r}) \rangle \right] \\ &= -\frac{\alpha q}{\varepsilon L} + 2 \times \frac{2\pi}{3\varepsilon\Omega} \int r^2 \rho_d(\mathbf{r}) d\mathbf{r}. \end{aligned} \quad (7)$$

This leads to a simple correction for the individual KS defect level, which relates to the total-energy correction via a prefactor of $-2/q$:

$$\varepsilon_{d,\text{corr}}^{\text{KS}} = -\frac{2}{q} E_{\text{corr}}. \quad (8)$$

To demonstrate our eigenvalue correction scheme, we consider finite-size effects for an F center in LiF, a prototypical

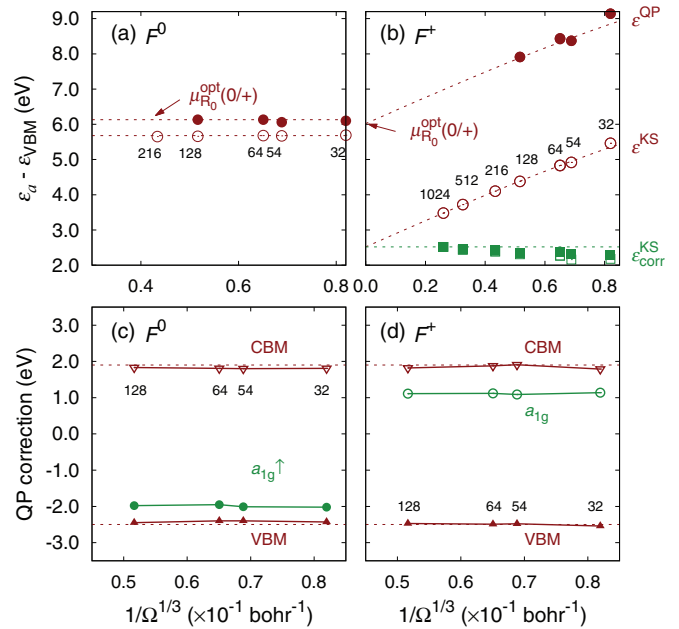


FIG. 3. (Color online) Finite-size scaling of the KS (open circles) and quasiparticle (closed circles) levels of the a_{1g} defect level for (a) the neutral F^0 and (b) the charged F^+ centers in LiF. In (b), the corrected KS eigenvalues are given with (closed squares) and without (open squares) the alignment term. The evolution of quasiparticle corrections of the a_{1g} level and of the band edges are shown for (c) F^0 and (d) F^+ . The band-edge quasiparticle corrections as obtained from a pristine bulk calculation are also shown (dashed). Both charge states are considered in the geometry of the neutral defect (R_0). The numbers of atomic sites in the supercells are indicated.

deep center which introduces a localized defect state of a_{1g} symmetry within the band gap. We use various supercells ranging from a 32-atom body-centered cubic to a 1024-atom simple cubic supercell. To minimize the effect of the dispersion of the PBE defect energy eigenvalue, we average its energy over the special \mathbf{k} points. The success of this procedure is demonstrated by the almost constant behavior of the a_{1g} level with increasing supercell size in the case of the neutral defect [Fig. 3(a)]. At variance, the unoccupied a_{1g} level of the positively charged F^+ exhibits a strong dependency on the supercell size. We perform an extrapolation to the dilute limit using the expression $a\Omega^{-1/3} + b\Omega^{-1} + c$, where Ω is the volume of the supercell.^{22,32} We note that for typical supercells used in G_0W_0 defect calculations (64 atoms), the a_{1g} level is higher than the extrapolation limit by over 2 eV. The slowly converging behavior of the defect level is eliminated by the correction given in Eq. (8). In particular, including the alignment term $\Delta V_{q/0}^{\text{DFT/pc}}$ accelerates the convergence for small supercells (Fig. 3).

To study finite-size effects of the quasiparticle correction, we perform G_0W_0 calculations for supercells containing up to 128 atoms. At variance with the behavior found for the eigenvalues, the quasiparticle corrections are largely invariant with respect to the supercell size [cf. Figs. 3(c) and 3(d)]. Thus, the finite-size effect needs to be considered only at the DFT level. Our G_0W_0 calculations additionally show that the quasiparticle corrections of the VBM and the conduction-band

TABLE III. G_0W_0 vertical transition energies $(q/q')_Q$ (in eV) of the defect levels calculated as ionization energy (IE) and electron affinity (EA) at the equilibrium geometry of the charge state Q . The energies are referred to the VBM.

	LiF:V _F		SiO ₂ :O _{int}	SiC:C _{sp}	
	(0/+) ₀	(0/+) ₊	(-/-) ₋	(0/+) ₀	(+/+) ₊
IE	6.13	8.76	4.96	1.30	1.18
EA	5.96	8.86	4.38	1.08	0.79

minimum (CBM) in the defect supercell closely correspond to those of the pristine bulk (Fig. 3), indicating that the supercell is sufficiently large to correctly reproduce the bulk properties.

B. Delocalization error

A second issue affecting the G_0W_0 defect levels concerns the calculation of the vertical excitation energy $\mu^{\text{opt}}(q/q - 1)$. Ideally, $\mu^{\text{opt}}(q/q - 1)$ can be calculated either as an ionization energy or as an electron affinity of the respective charge states $(q - 1)$ and q . However, in the G_0W_0 approximation, these two energies generally do not coincide.^{11,33} The origin of this effect is closely tied to the convex PBE starting point, which gives a strong delocalization error.³⁴ As shown in Table III, the magnitude of the delocalization error is generally small (~ 0.2 eV), but in some cases can reach values as high as 0.6 eV, as we find for the interstitial O in α -quartz. To reduce the delocalization error, we determine $\mu^{\text{opt}}(q/q - 1)$ as the mean value of the electron affinity and the ionization energy.¹¹ Interestingly, we note that calculating such average G_0W_0 vertical excitation energies including the eigenvalue corrections of Eq. (8) gives finite-size corrections coinciding with total-energy corrections used in DFT schemes.²³ Hence, adopting the proposed averaging scheme for the vertical transition ensures that the comparison between hybrid-functional and G_0W_0 energy levels is unaffected by the treatment of finite-size effects in either scheme.

C. Path dependence

The third issue of G_0W_0 calculations to which we devote attention concerns the combination of PBE relaxation energies and G_0W_0 quasiparticle energies to obtain thermodynamic charge transition levels $\mu(q/q')$ between charge states q and q' .⁵ The coupling of PBE and G_0W_0 gives rise to $\mu(q/q')$ that depends on the choice of path in configuration space (either $q \rightarrow q'$ or $q' \rightarrow q$).⁸ For the considered defects, we find differences of about 0.2 eV along the two paths (cf. Table IV). In addition, we evaluate the effect of relaxation energies with the two hybrid functionals. For LiF, PBE0 and HSE lead to a weaker path dependence, while for SiO₂ and SiC, the path dependence is enhanced with the hybrid functionals. To minimize the path dependence, we here determine $\mu(q/q')$ as an average over two paths. In this way, the calculation of $\mu(q/q')$ accounts for structural relaxation energies in both charge states q and q' . As seen in Table IV, the difference of charge transition levels due to the relaxation energies are now within 0.2 eV using the mean value.

TABLE IV. G_0W_0 charge transition levels (q/q') calculated along two paths for the presented defects. In path I (path II), the vertical excitation is taken from the equilibrium geometry of the charge state q (q'). The relaxation energies Δ are calculated using PBE, PBE0, and HSE functionals. The PBE geometries are used irrespective of the adopted functionals. δ accounts for the energy difference, and the averaged charge transition levels are given in the last column. The reported charge transition levels are referred to the VBM. Energies are in eV.

		Path I	Path II	δ	Mean
LiF:V _F (0/+)	Δ_{PBE}	7.73	7.95	0.22	7.84
	Δ_{PBE0}	7.91	7.89	0.02	7.90
	Δ_{HSE}	7.89	7.93	0.04	7.91
SiO ₂ :O _{int} (-/-)	Δ_{PBE}	4.38	4.62	0.24	4.50
	Δ_{PBE0}	4.31	5.06	0.75	4.68
	Δ_{HSE}	4.29	5.13	0.84	4.71
SiC:C _{sp} (0/+)	Δ_{PBE}	1.94	1.92	0.02	1.93
	Δ_{PBE0}	2.01	1.84	0.17	1.93
	Δ_{HSE}	2.10	1.85	0.25	1.97
(+/+)	Δ_{PBE}	1.63	1.14	0.49	1.38
	Δ_{PBE0}	1.68	1.13	0.55	1.40
	Δ_{HSE}	1.72	1.14	0.58	1.43

IV. CORRESPONDENCE OF DEFECT LEVELS IN VARIOUS SCHEMES

In Fig. 4, we present the thermodynamic charge transition levels for various point defects, as calculated in PBE, PBE0, HSE, and PBE + G_0W_0 . Upon the alignment of the electrostatic potentials of the bulk systems,^{1,2,4} a remarkable agreement between the predicted charge transition levels is immediately recognized. The PBE charge transition levels, while being much underestimated when referred to the respective VBM, are in excellent agreement with the G_0W_0 values, as manifested by a mean absolute deviation of only 0.17 eV. For the same alignment, the two hybrid functionals also give charge transition levels that are in excellent agreement with the G_0W_0 reference, showing even smaller mean absolute deviations of 0.08 (PBE0) and 0.10 eV (HSE). These results draw a strong connection between total-energy differences within the (generalized) KS schemes and G_0W_0 quasiparticle energies for charge transition levels of localized defects.

We note that for the O interstitial in α -quartz, the choice of paths is critical within the PBE + G_0W_0 scheme. In the ground state of the neutral interstitial O_{int}⁰, the first unoccupied σ^* state is promoted into the conduction band in the G_0W_0 calculation (Fig. 5). The vertical transition energy thereby corresponds to an electron addition to the σ^* state without filling the low-lying CBM, an electronic configuration that is unsustainable in standard DFT calculations. The thermodynamic charge transition levels $\mu(0/-)$ calculated starting from the neutral state (path I in Fig. 5) therefore suffers from a discontinuity Δ (cf. Fig. 5) due to the conflicting electronic configurations of PBE versus G_0W_0 . Consequently, the defect level $\mu(0/-)$ (5.88 eV) obtained from path I turns out to be unphysical and overestimated. This explains the high charge transition level reported in Ref. 9. At variance, $\mu(0/-)$ can be calculated safely along the alternative path II starting from the vertical transition

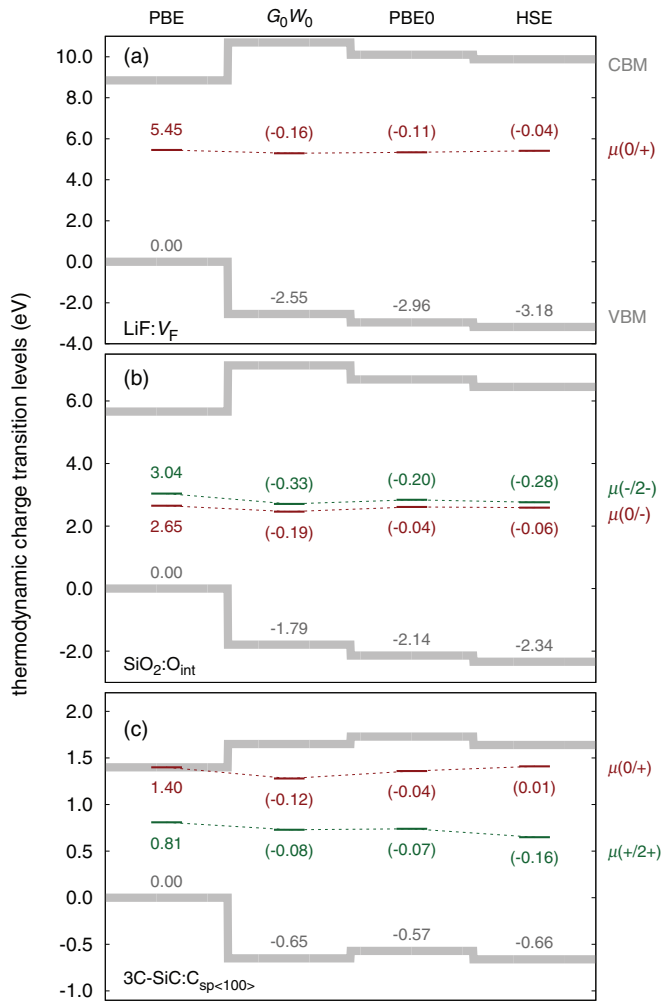


FIG. 4. (Color online) Thermodynamic charge transition levels of (a) LiF:V_F , (b) $\text{SiO}_2\text{:O}_\text{int}$, and (c) $3\text{C-SiC:}\text{C}_{\text{sp}(100)}$, as determined within PBE, PBE + G_0W_0 , PBE0, and HSE. The energy scales are aligned with respect to the electrostatic potential in the pristine bulk. The PBE VBM is set to zero. The values in parentheses show the shifts from the PBE charge transition levels.

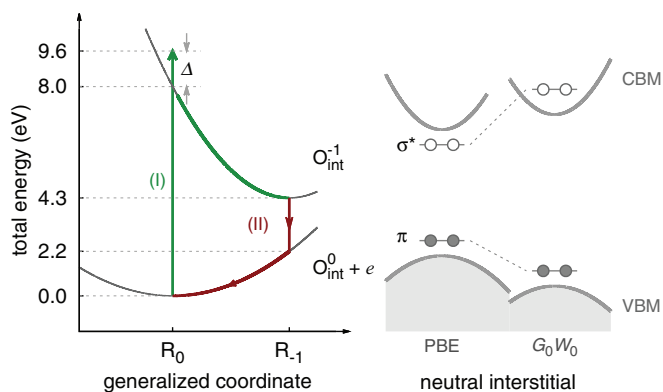


FIG. 5. (Color online) Left: Configuration coordinate diagram of the oxygen interstitial in α -quartz depicting two possible transition paths (I and II), as obtained in the PBE + G_0W_0 scheme. Right: Sketch of the electronic structures of the neutral defect in PBE and in G_0W_0 , showing the occupied (closed circles) and unoccupied (open circles) defect levels.

of $\text{O}_{\text{int}}^{-1}$ in its equilibrium position, as the localized defect state is then well situated in the band gap regardless of the adopted scheme. The revised G_0W_0 transition level (4.25 eV) restores the favorable comparison with those obtained from (hybrid) density functionals [Fig. 4(b)].

We then comment on the apparent discrepancy found by Jain *et al.*⁸ for their G_0W_0 defect levels of the O vacancy in HfO_2 as compared with previous hybrid-functional results.¹³ We focus on uncorrected results as we have demonstrated that finite-size effects lead to identical corrections in both kinds of calculations. From Ref. 8, we infer that the uncorrected defect levels $\mu(0/+)$ and $\mu(+/2+)$ occur at 3.96 and 3.86 eV from the VBM, respectively. Corresponding hybrid-functional levels in Ref. 13 are found at 4.12 and 4.06 eV. When the latter are aligned on the same energy scale as the G_0W_0 calculation,³⁵ they occur at 3.98 and 3.91 eV from the G_0W_0 VBM, respectively, within less than 0.05 eV from the G_0W_0 results.⁸ This close agreement further supports the correspondence between defect levels calculated with G_0W_0 and hybrid functionals. The origin of the discrepancy can thus entirely be confined to the different procedures adopted for the electrostatic correction.

We remark that the established correspondence of localized defect levels is inherently associated with the reliable ionization (affinity) energies of isolated species obtained from total-energy differences within DFT.³⁷ In addition, while we use PBE for the reference orbitals of the perturbative G_0W_0 calculation, the agreement is robust against the choice of a different starting point (e.g., a hybrid functional). This is supported by Refs. 38 and 39 showing that G_0W_0 calculations on top of the PBE and PBE0 starting points agree within 0.3–0.4 eV for the ionization energies of a series of molecules. Caruso *et al.* further show that a fully consistent GW treatment of the ionization energies also leads to results comparable to G_0W_0 .³⁹ Overall, we expect the correspondence of defect energy levels not to be affected by the various GW flavors when the electrostatic potential reference is used.

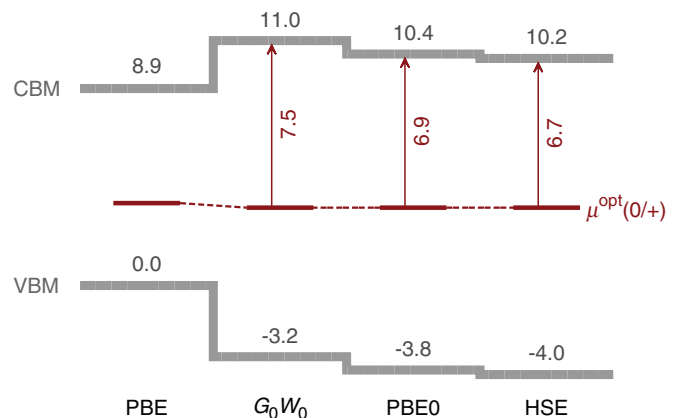


FIG. 6. (Color online) Vertical charge transition levels $\mu^{\text{opt}}(0/+)$ of LiF:F^0 (at the neutral defect geometry) calculated within PBE, G_0W_0 , PBE0, and HSE. The G_0W_0 and hybrid-functional calculations reproduce the experimental band gap (14.2 eV). The energy levels are aligned with respect to the electrostatic potential of the pristine bulk. Energies are in eV.

TABLE V. Vertical transition energies $\Delta E = \varepsilon_{\text{CBM}} - \mu^{\text{opt}}(0/+)$ between the defect level $\mu^{\text{opt}}(0/+)$ of the F^0 center in LiF and the CBM (ε_{CBM}), as obtained in the PBE0, HSE, and G_0W_0 schemes. The effect of the excitonic binding energy is also considered ($E_b = 1.9$ eV). The experimental result is taken from Ref. 36. Energies are in eV.

	G_0W_0	PBE0	HSE	Expt.
ΔE	7.5	6.9	6.7	
$\Delta E - E_b$	5.6	5.0	4.8	5.0

Unlike for localized defect states, the energy levels of delocalized band-edge states exhibit strong variations with the adopted electronic-structure method (cf. Fig. 4).^{34,40} The position of the calculated band edges directly affects the comparison with experiment. To illustrate the role of the band-edge positions, we here focus on the F center in LiF. The F center in LiF is at the origin of a peak at 5.0 eV in the optical absorption spectrum,³⁶ corresponding to a vertical excitation from the neutral defect level $\mu^{\text{opt}}(0/+)$ to the conduction band edge. By varying the initial electronic-structure configuration in the G_0W_0 and the fraction of Fock exchange in the hybrid functionals, we achieve theoretical descriptions all reproducing the experimental band gap. Specifically, the G_0W_0 calculation starts from a PBE0 calculation in which the fraction of Fock exchange α is set to 0.20. The band gaps in the PBE0 and HSE calculations can similarly be tuned to match the experimental band gap by setting α to 0.45 and 0.59, respectively. Figure 6 shows that the various schemes yield close positions for $\mu^{\text{opt}}(0/+)$, while the associated band structures show relative shifts up to 0.8 eV. To enable the comparison with the experimental absorption energy, we take into account the excitonic binding energy ($E_b = 1.9$ eV, see Appendix B for details), which is subtracted from the vertical transition energies $\Delta E = \varepsilon_{\text{CBM}} - \mu^{\text{opt}}(0/+)$. As shown in Table V, the various schemes do not yield equivalent results. PBE0 (5.0 eV) scores the best agreement with the experimental value of 5.0 eV,³⁶ whereas G_0W_0 gives an overestimation of 0.6 eV. While this case study illustrates the importance of achieving accurate band-edge positions, a general assessment of the performance of various electronic-structure methods requires the consideration of a larger variety of systems.

V. CONCLUSIONS

A close correspondence has been demonstrated between hybrid-functional and G_0W_0 determinations of charge transition levels for atomically localized defects. In particular, we resolve discrepancies previously pointed out in the literature and show that they are not directly related to the accuracy of the adopted electronic-structure method. Unlike defect levels, the energy levels of delocalized band states show a much higher sensitivity and represent the real bottleneck for defect-level predictions of high accuracy.

ACKNOWLEDGMENTS

We acknowledge useful interactions with P. Broqvist, H.-P. Komsa, and G.-M. Rignanese. We used computational resources of CSEA-EPFL and CSCS. Partial support from

the Swiss National Science Foundation is also acknowledged (Grant No. 206021-128743).

APPENDIX A: FINITE-SIZE CORRECTION OF THE TOTAL ENERGY FOR A CHARGED DEFECT SUPERCELL

In this Appendix, we formulate the electrostatic correction for a localized charged defect in a supercell following the scheme proposed by Freysoldt, Neugebauer, and Van de Walle.^{23,24} In the original scheme,^{23,24} a localized model charge $\rho^{\text{mod}}(\mathbf{r})$ is used to represent the actual defect charge distribution

$$q = \int \rho^{\text{mod}}(\mathbf{r}) d\mathbf{r}. \quad (\text{A1})$$

The model charge gives rise to a long-range electrostatic potential

$$V^{\text{mod}}(\mathbf{r}) = \int \frac{\rho^{\text{mod}}(\mathbf{r}')}{\varepsilon|\mathbf{r} - \mathbf{r}'|} d\mathbf{r}', \quad (\text{A2})$$

where ε is the macroscopic dielectric constant of the medium. The correction corresponds to the spurious interactions due to the periodic images and the neutralizing background, and it can be expressed as²²⁻²⁴

$$E_{\text{corr}} = E_{\text{iso}}^{\text{mod}} - E_{\text{per}}^{\text{mod}} - q\Delta V_{q/0}^{\text{DFT/mod}}, \quad (\text{A3})$$

where $E_{\text{iso}}^{\text{mod}}$ is the self-energy of the isolated model charge

$$E_{\text{iso}}^{\text{mod}} = \frac{1}{2} \iint \frac{\rho^{\text{mod}}(\mathbf{r})\rho^{\text{mod}}(\mathbf{r}')}{\varepsilon|\mathbf{r} - \mathbf{r}'|} d\mathbf{r} d\mathbf{r}'. \quad (\text{A4})$$

For a spherical charge distribution, $E_{\text{iso}}^{\text{mod}}$ can be calculated in reciprocal space as

$$E_{\text{iso}}^{\text{mod}} = \frac{1}{\pi\varepsilon} \int [\rho^{\text{mod}}(k)]^2 dk, \quad (\text{A5})$$

where $\rho^{\text{mod}}(k)$ is the Fourier transform of $\rho^{\text{mod}}(\mathbf{r})$

$$\rho^{\text{mod}}(k) = \rho^{\text{mod}}(\mathbf{k}) = \int \rho^{\text{mod}}(\mathbf{r}) \exp(-i\mathbf{k} \cdot \mathbf{r}) d\mathbf{r}. \quad (\text{A6})$$

$E_{\text{per}}^{\text{mod}}$ is the periodic energy including both the self-energy and the interaction with the periodic images and the background jellium,

$$E_{\text{per}}^{\text{mod}} = \frac{2\pi}{\varepsilon\Omega} \sum_{\mathbf{G} \neq 0} \frac{[\rho^{\text{mod}}(|\mathbf{G}|)]^2}{|\mathbf{G}|^2}, \quad (\text{A7})$$

where Ω is the volume of the supercell, and \mathbf{G} a reciprocal lattice vector. The residual local field effects due to microscopic screening are accounted for by a potential alignment

$$\Delta V_{q/0}^{\text{DFT/mod}} = \underbrace{V_q^{\text{DFT}} - V_0^{\text{DFT}}}_{V_{q/0}^{\text{DFT}}} - V^{\text{mod}}, \quad (\text{A8})$$

evaluated in the region far away from the defect. An illustration of the associated potential profiles is given in Fig. 7 for an F^+ center in LiF.

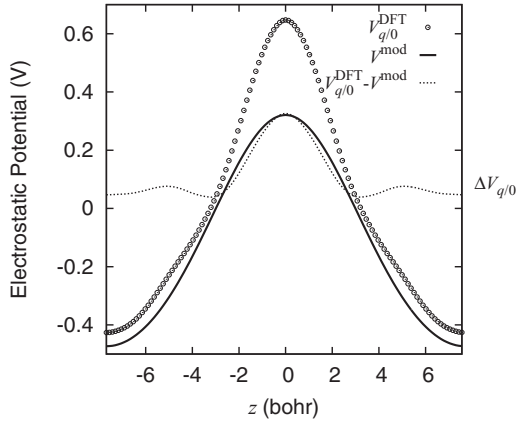


FIG. 7. The electrostatic-potential profile for an F^+ center in LiF. The vacancy is at the origin.

In this work, we use E_{corr} expressed in terms of the Madelung energy of a point charge (pc) embedded in a dielectric $E_{\text{Mad}}^{\text{pc}}$ (Ref. 24):

$$E_{\text{corr}} = E_{\text{Mad}}^{\text{pc}} - q \Delta V_{q/0}^{\text{DFT/pc}}, \quad (\text{A9})$$

where $\Delta V_{q/0}^{\text{DFT/pc}}$ is the alignment between the DFT potential and the point-charge potential. The latter can be expressed through the model charge alignment as

$$\Delta V_{q/0}^{\text{DFT/pc}} = \Delta V_{q/0}^{\text{DFT/mod}} + \Delta V^{\text{mod/pc}}, \quad (\text{A10})$$

where $\Delta V^{\text{mod/pc}}$ is the alignment between the potential of the adopted model charge and that of a point charge:²²

$$\begin{aligned} -\Delta V^{\text{mod/pc}} &= \frac{1}{\Omega} \int \left[V^{\text{mod}}(\mathbf{r}) - \frac{q}{\epsilon r} \right] d\mathbf{r} \\ &= -\frac{2\pi}{3\epsilon\Omega} \int 4\pi r^4 \rho^{\text{mod}}(r) dr \\ &= \frac{2\pi}{\epsilon\Omega} \left. \frac{\partial^2 \rho^{\text{mod}}(k)}{\partial k^2} \right|_{k=0} \\ &= V^{\text{mod}}(\mathbf{G} = 0). \end{aligned} \quad (\text{A11})$$

For cubic supercells, the correction is conveniently written as

$$E_{\text{corr}} = \frac{\alpha q^2}{2\epsilon L} - q \Delta V_{q/0}^{\text{DFT/pc}}, \quad (\text{A12})$$

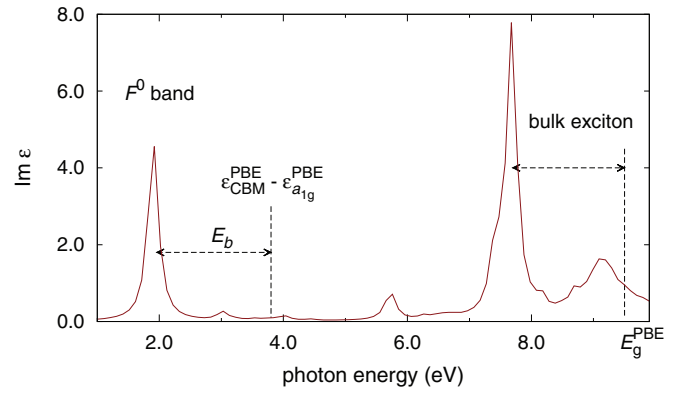


FIG. 8. (Color online) Optical absorption spectrum of LiF: F^0 calculated by solving the Bethe-Salpeter equation. The absorption peak at 1.9 eV is assigned to the F^0 band. The peak at 7.7 eV is assigned to bulk absorption.

where $E_{\text{Mad}}^{\text{pc}}$ has been replaced by the expression proposed by Leslie and Gillan.²⁵

APPENDIX B: EXCITONIC BINDING ENERGY OF THE F^0 CENTER IN LiF

We evaluate the excitonic binding energy E_b associated with the excitation of the unpaired electron to the CBM in the presence of a neutral F^0 center in LiF. We solve the two-particle Bethe-Salpeter equation based on a PBE determination of the electronic structure. The calculation is performed for a 31-atom body-centered-cubic supercell with a neutral vacancy. To construct the Bethe-Salpeter (BS) kernel, we include 17 occupied and 13 unoccupied states. We adopt the Tamm-Dancoff approximation, which consists in neglecting the antiresonant part in the Bethe-Salpeter kernel.⁴¹ A $4 \times 4 \times 4$ \mathbf{k} -point mesh is used for the BS calculation. Two prominent peaks are visible in the absorption spectrum shown in Fig. 8. At 7.7 eV, the strong absorption peak results from the VBM-CBM transition. The other absorption peak at 1.9 eV arises from the a_{1g} -CBM transition, which is assigned to the F^0 band absorption. Note that this transition energy occurs at 3.8 eV at the PBE level, as obtained from the Kohn-Sham eigenvalue difference $\epsilon_{\text{CBM}} - \epsilon_{a_{1g}}$. From the red-shift, we thus infer an excitonic binding energy of 1.9 eV.

¹A. Alkauskas, P. Broqvist, and A. Pasquarello, *Phys. Status Solidi B* **248**, 775 (2011).

²A. Alkauskas, P. Broqvist, and A. Pasquarello, *Phys. Rev. Lett.* **101**, 046405 (2008).

³A. J. Cohen, P. Mori-Sánchez, and W. Yang, *Phys. Rev. B* **77**, 115123 (2008).

⁴A. Alkauskas and A. Pasquarello, *Phys. Rev. B* **84**, 125206 (2011).

⁵M. Hedström, A. Schindlmayr, G. Schwarz, and M. Scheffler, *Phys. Rev. Lett.* **97**, 226401 (2006); P. Rinke, A. Janotti, M. Scheffler, and C. G. Van de Walle, *ibid.* **102**, 026402 (2009).

⁶L. Hedin, *Phys. Rev.* **139**, A796 (1965).

⁷M. S. Hybertsen and S. G. Louie, *Phys. Rev. B* **34**, 5390 (1986).

⁸M. Jain, J. R. Chelikowsky, and S. G. Louie, *Phys. Rev. Lett.* **107**, 216803 (2011).

⁹L. Martin-Samos, G. Roma, P. Rinke, and Y. Limoge, *Phys. Rev. Lett.* **104**, 075502 (2010).

¹⁰S. Lany and A. Zunger, *Phys. Rev. B* **81**, 113201 (2010).

¹¹F. Bruneval, *Phys. Rev. Lett.* **103**, 176403 (2009).

¹²M. Bockstedte, A. Marini, O. Pankratov, and A. Rubio, *Phys. Rev. Lett.* **105**, 026401 (2010).

¹³P. Broqvist and A. Pasquarello, *Appl. Phys. Lett.* **89**, 262904 (2006).

- ¹⁴*Advanced Calculations for Defects in Materials*, edited by A. Alkauskas, P. Deák, J. Neugebauer, A. Pasquarello, and C. G. Van de Walle (Wiley, Weinheim, 2011).
- ¹⁵J. P. Perdew, K. Burke, and M. Ernzerhof, *Phys. Rev. Lett.* **77**, 3865 (1996).
- ¹⁶P. Giannozzi, S. Baroni, N. Bonini, M. Calandra, R. Car, C. Cavazzoni, D. Ceresoli, G. L. Chiarotti, M. Cococcioni, I. Dabo, A. Dal Corso, S. de Gironcoli, S. Fabris, G. Fratesi, R. Gebauer, U. Gerstmann, C. Gougoussis, A. Kokalj, M. Lazzeri, L. Martin-Samos, N. Marzari, F. Mauri, R. Mazzarello, S. Paolini, A. Pasquarello, L. Paulatto, C. Sbraccia, S. Scandolo, G. Sclauzero, A. P. Seitsonen, A. Smogunov, P. Umari, and R. M. Wentzcovitch, *J. Phys.: Condens. Matter* **21**, 395502 (2009).
- ¹⁷J. P. Perdew, M. Ernzerhof, and K. Burke, *J. Chem. Phys.* **105**, 9982 (1996).
- ¹⁸J. Heyd, G. E. Scuseria, and M. Ernzerhof, *J. Chem. Phys.* **118**, 8207 (2003); **124**, 219906 (2006).
- ¹⁹H.-P. Komsa, P. Broqvist, and A. Pasquarello, *Phys. Rev. B* **81**, 205118 (2010).
- ²⁰P. Broqvist, A. Alkauskas, and A. Pasquarello, *Phys. Rev. B* **80**, 085114 (2009).
- ²¹C. G. Van de Walle and J. Neugebauer, *J. Appl. Phys.* **95**, 3851 (2004).
- ²²H.-P. Komsa, T. T. Rantala, and A. Pasquarello, *Phys. Rev. B* **86**, 045112 (2012).
- ²³C. Freysoldt, J. Neugebauer, and C. G. Van de Walle, *Phys. Rev. Lett.* **102**, 016402 (2009).
- ²⁴C. Freysoldt, J. Neugebauer, and C. G. Van de Walle, *Phys. Status Solidi B* **248**, 1067 (2011).
- ²⁵M. Leslie and M. J. Gillan, *J. Phys. C: Solid State Phys.* **18**, 973 (1985).
- ²⁶P. E. Blöchl, *Phys. Rev. B* **50**, 17953 (1994).
- ²⁷X. Gonze, B. Amadon, P.-M. Anglade, J.-M. Beuken, F. Bottin, P. Boulanger, F. Bruneval, D. Caliste, R. Caracas, M. Ct, T. Deutsch, L. Genovese, P. Ghosez, M. Giantomassi, S. Goedecker, D. Hamann, P. Hermet, F. Jollet, G. Jomard, S. Leroux, M. Mancini, S. Mazevet, M. Oliveira, G. Onida, Y. Pouillon, T. Rangel, G.-M. Rignanese, D. Sangalli, R. Shaltaf, M. Torrent, M. Verstraete, G. Zerah, and J. Zwanziger, *Comput. Phys. Commun.* **180**, 2582 (2009).
- ²⁸R. W. Godby and R. J. Needs, *Phys. Rev. Lett.* **62**, 1169 (1989).
- ²⁹C. Friedrich, M. C. Müller, and S. Blügel, *Phys. Rev. B* **83**, 081101 (2011).
- ³⁰S. E. Taylor and F. Bruneval, *Phys. Rev. B* **84**, 075155 (2011).
- ³¹I. Dabo, B. Kozinsky, N. E. Singh-Miller, and N. Marzari, *Phys. Rev. B* **77**, 115139 (2008).
- ³²C. W. M. Castleton, A. Höglund, and S. Mirbt, *Phys. Rev. B* **73**, 035215 (2006).
- ³³F. Bruneval, *Nucl. Instrum. Methods Phys. Res., Sect. B* **277**, 77 (2012).
- ³⁴P. Mori-Sánchez, A. J. Cohen, and W. Yang, *Phys. Rev. Lett.* **100**, 146401 (2008).
- ³⁵From our own calculations, we infer that the VBM in the hybrid-functional calculation lies lower than the G_0W_0 VBM by 0.15 eV.
- ³⁶M. R. Mayhugh, *J. Appl. Phys.* **41**, 4776 (1970).
- ³⁷O. A. Vydrov and G. E. Scuseria, *J. Chem. Phys.* **122**, 184107 (2005).
- ³⁸F. Bruneval and M. A. L. Marques, *J. Chem. Theory Comput.* **9**, 324 (2013).
- ³⁹F. Caruso, P. Rinke, X. Ren, A. Rubio, and M. Scheffler, *Phys. Rev. B* **88**, 075105 (2013).
- ⁴⁰W. Chen and A. Pasquarello, *Phys. Rev. B* **86**, 035134 (2012).
- ⁴¹G. Onida, L. Reining, and A. Rubio, *Rev. Mod. Phys.* **74**, 601 (2002).